

XMM-Newton observations of the diffuse X-ray emission in the starburst galaxy NGC 253[★]

M. Bauer¹, W. Pietsch¹, G. Trinchieri², D. Breitschwerdt³, M. Ehle⁴, M.J. Freyberg¹ and A. Read⁵

¹ Max-Planck-Institut für extraterrestrische Physik, Giessenbachstraße, 85741 Garching, Germany

² INAF Osservatorio Astronomico di Brera, via Brera 28, 20121 Milano, Italy

³ Institut für Astronomie der Universität Wien, Türkenschanzstr. 17, A-1180 Wien, Austria

⁴ XMM-Newton Science Operations Centre, ESA, P.O. Box 78, 28691 Villanueva de la Cañada, Madrid, Spain

⁵ Department of Physics & Astronomy, University of Leicester, Leicester LE1 7RH, UK

Received XX XX 2007; accepted XX XX 2007.

ABSTRACT

Aims. We present a study of the diffuse X-ray emission in the halo and the disc of the starburst galaxy NGC 253.

Methods. After removing point sources, we analysed *XMM-Newton* images, hardness ratio maps and spectra from several regions in the halo and the disc. We introduce a method to produce vignetting corrected images from the EPIC PN data, and we developed a procedure that allows a correct background treatment for low surface brightness spectra, using a local background, together with closed filter observations.

Results. Most of the emission from the halo is at energies below 1 keV. In the disc, also emission at higher energies is present. The extent of the diffuse emission along the major axis of the disc is 13.6 kpc. The halo resembles a horn structure and reaches out to ~9 kpc perpendicular to the disc. Disc regions that cover star forming regions, like spiral arms, show harder spectra than regions with lower star forming activity. Models for spectral fits of the disc regions need at least three components: two thermal plasmas with solar abundances plus a power law and galactic foreground absorption. Temperatures are between 0.1 and 0.3 keV and between 0.3 and 0.8 keV for the soft and the hard component, respectively. The power law component may indicate an unresolved contribution from X-ray binaries in the disc. The halo emission is not uniform, neither spatially nor spectrally. The southeastern halo is softer than the northwestern halo. To model the spectra in the halo, we needed two thermal plasmas with solar abundances plus galactic foreground absorption. Temperatures are around 0.1 and 0.3 keV. A comparison between X-ray and UV emission shows that both originate from the same regions. The UV emission is more extended in the southeastern halo, where it seems to form a shell around the X-ray emission.

Key words. X-rays: galaxies – X-rays: ISM – Galaxies: individual: NGC 253 – Galaxies: halos – Galaxies: ISM – Galaxies: starburst

1. Introduction

The diffuse X-ray emission of starburst galaxies can be quite prominent. Especially in galaxies that we see edge-on, we can find very complex emission from galactic halos. One famous example is the starburst galaxy NGC 253 in the Sculptor Group. It is close enough (2.58 Mpc, $l' = 750$ pc, Puche et al. 1991) to resolve structures in the disc and halo, and to separate the detected point sources from the diffuse emission. Also, it is seen almost edge-on (78.5° , Pence 1980), so an unobscured analysis of the halo emission is possible. NGC 253 has been observed in X-rays many times. There are observations with *Einstein* (e.g. Fabbiano & Trinchieri 1984), *ROSAT* (e.g. Pietsch 1992; Read et al. 1997; Dahlem et al.

1998; Vogler & Pietsch 1999; Pietsch et al. 2000), *ASCA* (e.g. Ptak et al. 1997), *BeppoSAX* (e.g. Cappi et al. 1999), *XMM-Newton* (e.g. Pietsch et al. 2001; Bauer et al. 2007), and *Chandra* (e.g. Weaver et al. 2002; Strickland et al. 2002, 2004a,b). While with some instruments one was not able to separate emission from point sources and diffuse emission, other instruments, especially *ROSAT*, *XMM-Newton*, and *Chandra*, do have a narrow enough point spread function to do so. We here report on the first extensive analysis of the diffuse emission in NGC 253 with *XMM-Newton*.

2. Observations and data reduction

NGC 253 was observed with *XMM-Newton* (Jansen et al. 2001) during three orbits in June 2000 and June 2003, using all of the European Photon Imaging Camera (EPIC) instruments (Strüder et al. 2001; Turner et al. 2001), the two co-aligned RGS spectrometers, RGS1 and RGS2 (den Herder et al. 2001),

Send offprint requests to: M. Bauer, e-mail: mbauer@mpe.mpg.de

[★] Based on observations obtained with XMM-Newton, an ESA science mission with instruments and contributions directly funded by ESA Member States and NASA

Table 1. *XMM-Newton* EPIC PN NGC 253 observation log.

Nr.	Revolution number	Obs. id.	Obs. dates	Pointing direction RA/DEC (J2000)		P. A. (deg)	Filter	T _{exp} (ks)	T _{exp, clean} (ks)
(1)	(2)	(3)	(4)	(5)	(6)	(7)	(8)	(9)	(10)
1	89	0125960101	2000-06-03	00:47:36.74	-25:17:49.2	56.9	Medium	60.8	24.3
2	89	0125960201	2000-06-04	00:47:36.57	-25:17:48.7	57.0	Thin	17.5	3.1
3	186	0110900101	2000-12-14	00:47:30.20	-25:15:53.2	233.8	Thin	24.4	4.4
4	646	0152020101	2003-06-19	00:47:36.89	-25:17:57.3	53.8	Thin	113.0	47.9

and the Optical Monitor (Mason et al. 2001), for a total of about 216 ks. The revolution number, observation identifier, observing date, pointings and orientation of the satellite (P.A.), and the total exposure times for the EPIC PN camera (T_{exp}) are shown in Table 1.

Throughout the following analysis, we used the MOS data *only* to detect and remove point sources. We were especially interested in low-surface brightness diffuse emission at energies below 1 keV, where the MOS detectors have a lower sensitivity than the EPIC PN. By not utilising the MOS data for the analysis of the diffuse emission, we avoided a higher background noise level.

We analysed the data using the Science Analysis System (SAS), version 7.0.0. In a first step, we cleaned the EPIC PN and MOS observations by excluding times, where the count rate over the whole detector above 10 keV exceeded the count rate during quiescent times. This cleaning was done to avoid times with high particle background, which result in a higher background level. The observations showed no obvious additional times with solar wind charge exchange (e.g. Snowden et al. 2004), which would result in times with high background at energies below 1 keV, so no further exclusion of exposure time was necessary. The exposure times after screening for high background (T_{exp, clean}) are shown in Table 1. Summing up over the final good time intervals, we ended up with 80 ks of exposure time in total. This means only about 37% of the original exposure time could be used for the analysis presented in this paper. This number is quite small, compared to typical exposure time fractions of usable times after screening of 60–70%¹. Next, we screened for bad pixels that were not detected by the pipeline. In order to be able to merge images later on, we calculated sky coordinates (X,Y) for the events in all observations with respect to the centre reference position $\alpha_{2000}=00^{\text{h}}47^{\text{m}}33^{\text{s}}.3$, $\delta_{2000}=-25^{\circ}17'18''$. For the following analysis we split the data set into five energy bands: 0.2–0.5 keV, 0.5–1.0 keV, 1.0–2.0 keV, 2.0–4.5 keV and 4.5–12 keV as bands 1 to 5.

2.1. Point source removal

In this paper we did not study the population of the point sources, but we focused on the diffuse emission in the halo and the disc of the galaxy. To do so, we had to remove con-

tributions from point sources. In order to run the source detection algorithm of the SAS-software package, we created images for the PN, selecting only single events (PATTERN=0) in energy band 1, and single and double events (PATTERN≤4) for the other bands. For MOS we used single to quadruple events (PATTERN≤12) in all bands. To avoid differences in the background over the PN detector, we omitted the energy range between 7.2 keV and 9.2 keV, where the detector background shows strong spatially variable fluorescence lines (Freyberg et al. 2004). We created images, background images and exposure maps, and masked them to an acceptable detector area. The binning for all images is 2".

We searched for point sources in the field of view (FOV), simultaneously in the 5 energy bands and three detectors. First, we searched in each observation separately, to correct for inaccuracies in the pointing positions. The resulting source lists were correlated to catalogues from USNO (Monet et al. 2003), SIMBAD², and *Chandra* (Strickland et al. 2002). Offsets were determined and applied to each observation. With the position corrected event files, we again created images on which we executed the final point source detection. We searched in the merged images from observations 1, 2, and 4, and separately in the images from observation 3. The reason for merging only observations 1, 2 and, 4 is that observation 3 has a pointing offset (~6') into the northwestern halo and therefore we would have different point spread functions on the same sky coordinates.

Additionally, we created a point source catalogue for the *Chandra* observations. Point sources in *Chandra*ObsID 3931 were identified using the Wavelet-Based detection Algorithm (wavdetect in the *ciao* software, version 3.4, Freeman et al. 2002), in the 0.5–5.0 keV energy band using scales of 1", 2", 4", 8", and 16". For ObsID 969 and ObsID 790 we adopted the published source list from Strickland et al. (2002). The combined *XMM-Newton* and *Chandra* source list will be published and further discussed in a forthcoming paper.

The combined source list was used to remove the point sources from the data sets. The SAS-task `region` was used to produce elliptical regions that approximate the PSF with an analytical model at a given detector position and flux value (0.5 times the background flux at this position). Sources that were not detected in the *XMM-Newton* data sets, but are known from *Chandra* observations, were excluded with a circular region

¹ see the *XMM-Newton* EPIC Background Working Group webpage <http://www.star.le.ac.uk/~amr30/BG/BGTable.html>

² <http://simbad.u-strasbg.fr/simbad/>

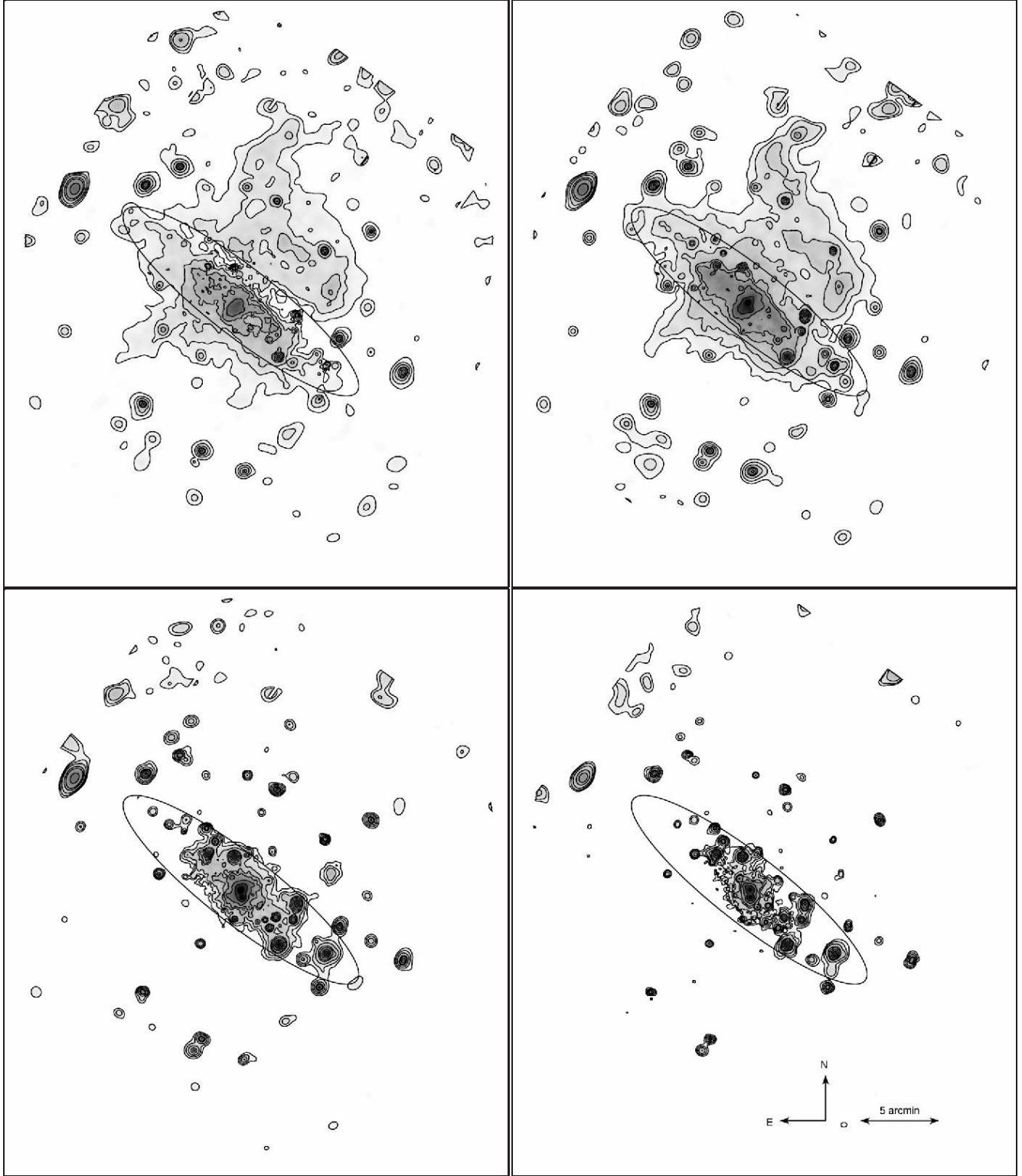


Fig. 1. Adaptively smoothed EPIC PN images with contours in the lower 4 energy bands: (top-left) 0.2–0.5 keV, (top-right) 0.5–1.0 keV, (bottom-left) 1.0–2.0 keV, and (bottom-right) 2.0–4.5 keV. Contours are at $(0.35, 0.50, 0.80, 1.6, 2.5, 6.0, 20, 100) \times 10^{-5} \text{ ct s}^{-1} \text{ pix}^{-1}$. Additionally we show the inclination corrected optical D_{25} ellipse in black.

with a diameter of $8''$. One might argue that these sources contribute only little to the overall emission. However, we took up a conservative position and also excluded these sources to keep any unwanted interference at a minimum. An extended source,

most likely a galaxy cluster candidate in the background was additionally masked with a circular region of $1.5'$ diameter.

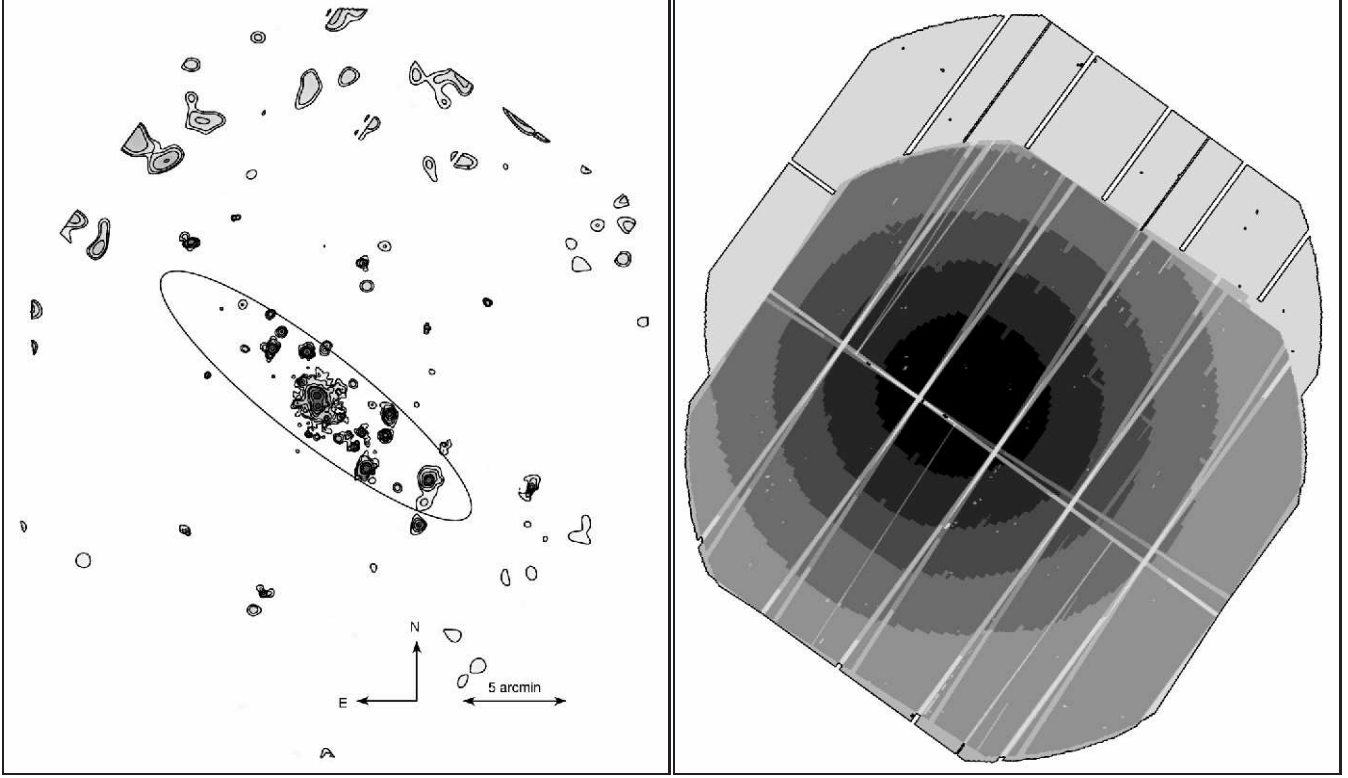


Fig. 2. (*left*): Adaptively smoothed EPIC PN image with contours in the highest different energy band (4.5–12 keV). Contour levels are the same as in Fig. 1. (*right*): The vignetting corrected exposure map of the merged four observations. The outer contour indicates 0 ks and the exposure increases linearly towards the centre by one seventh of the maximum (80 ks) per gray-scale level (0–11.4 ks, 11.4–22.9 ks, 22.9–34.3 ks, 34.3–45.7 ks, 45.7–57.1 ks, 57.1–68.6 ks, 68.6–80.0 ks). Except for a few pixels, all the detector gaps are covered by at least 4.4 ks in the central region.

2.2. Images

We used all 4 observations to produce images. The observations have different pointing directions and position angles, so we obtained images where almost all the CCD gaps are filled. The single images, from the energy bands 1 to 5, were corrected for the detector background (electronic noise, high energy particles) by subtracting the surface brightness of the detector corners, that are outside of the field of view. The images were exposure and vignetting corrected, and adaptively smoothed with a Gaussian kernel, with sizes between $10''$ and $47''$ (Fig. 1 and 2). For a detailed description of this method see App. B. A false-colour image was produced by combining the three lowest energy bands 1, 2, and 3, as channels red, green, and blue, respectively (Fig. 3). The image, after the point source removal is shown in Fig. 4.

2.3. Hardness ratio maps and spectra

As a big advantage, compared to the observations by *ROSAT* and *Chandra*, the higher count rates in *XMM-Newton* allowed us to extract spectra with reasonable statistics from smaller regions in the disc and the halo. For the hardness ratios and spectra we again restricted ourselves to the EPIC PN data. We did not use observations 2 and 3 for hardness ratios and spectra, because after good time interval screening only little exposure was left (cf. Table 1).

Energy spectra of several regions (cf. Fig. 4) were extracted from the event files after removal of the point sources. To calculate the area of these regions, we used the task *backscale*. We produced background spectra using a region at the south-western border of the FOV, together with observations where the filter wheel was closed. A detailed description of this procedure, which also handles the binning of the spectra, can be found in Appendix C. The final, background subtracted source spectrum for each region has a significance of at least 3σ in each data bin.

Since the emission is mostly confined to energies between 0.2 and 2.0 keV, we only calculated the hardness ratios HR1 and HR2, where $HR1 = (B_2 - B_1) / (B_2 + B_1)$, and $HR2 = (B_3 - B_2) / (B_3 + B_2)$. B_1 , B_2 , and B_3 are the count rates in the energy bands 1 to 3, i.e. 0.2–0.5 keV, 0.5–1.0 keV, and 1.0–2.0 keV, respectively. They were obtained by summing up the background subtracted counts in the spectra in the energy bands and observations.

In order to fit the spectra with physical models, we created the proper response and auxiliary response files for extended sources for each spectrum. In XSPEC 11.3.2, we linked the model parameters between the two observations and included a global renormalisation factor to account for differences between the observations to fit the spectra from observations 1 and 4 simultaneously.

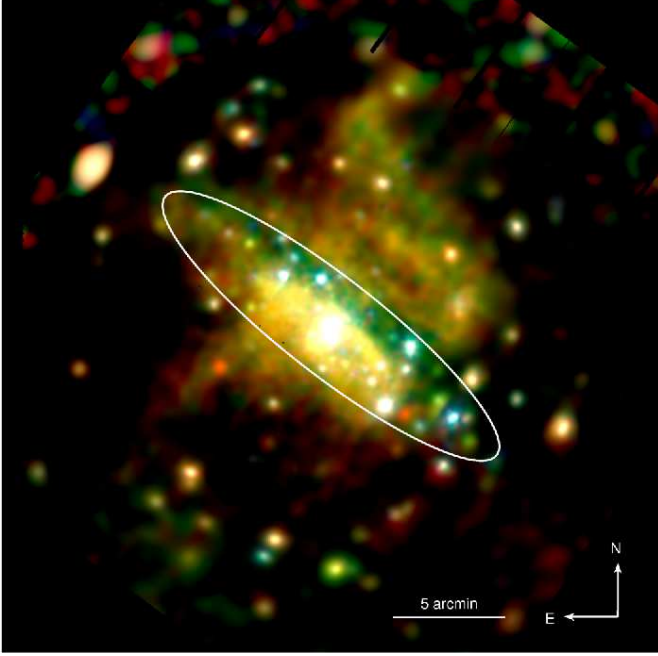


Fig. 3. Adaptively smoothed EPIC PN image of NGC 253. The colours correspond to the energy bands (0.2–0.5 keV, red), (0.5–1.0 keV, green), and (1.0–2.0 keV, blue). Overplotted in white is the inclination corrected optical D_{25} ellipse of NGC 253. Scale and orientation are indicated.

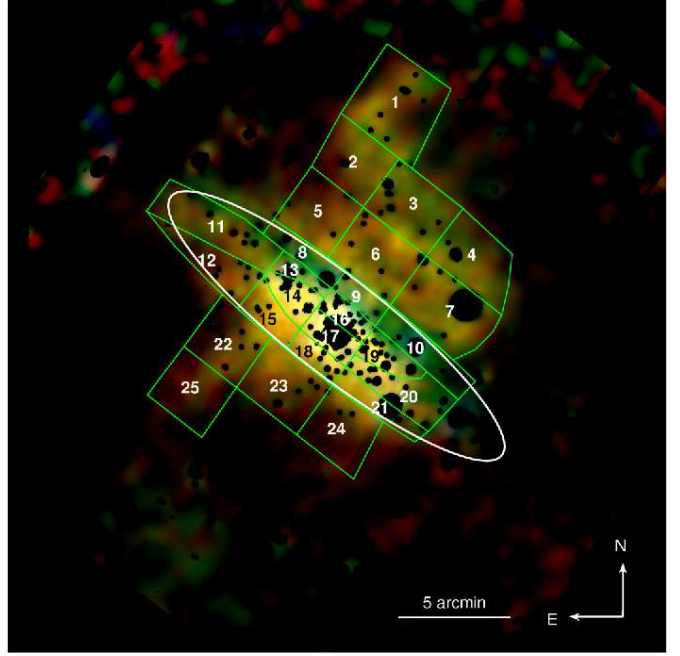


Fig. 4. Adaptively smoothed EPIC PN image of the diffuse emission of NGC 253. Point sources have been removed. Overplotted in green are the regions that were used for extracting hardness ratios and spectra. The inclination corrected optical D_{25} ellipse is shown in white.

3. Results

To characterise the diffuse emission in the disc and the halo, we analysed images in different energy bands, and hardness ratios and spectra from several regions. In the disc the regions were chosen in a way that they follow the spiral arm structure. In the halo, we chose plane-parallel regions above the galactic disc. The projected heights of the halo regions are 2 kpc, with exception of the region furthest to the northwest (region 1), which has a projected height of 3 kpc. The regions are overplotted on top the false-colour X-ray image in Fig. 4. The hardness ratios in the different regions are given in Table A.1 and shown graphically in Fig. 5.

3.1. Disc diffuse emission

The disc shows diffuse emission in energies up to ~ 10 keV, where the harder emission is located close to the centre of NGC 253. The soft emission (< 1 keV) shows the largest extent along the major axis. From the nucleus, it reaches ~ 7.0 kpc to the northwest and ~ 6.4 kpc to the southeast.

A prominent feature in the disc is the lack of very soft emission northwest of the major axis. This is already known from *ROSAT* observations (e.g. Pietsch et al. 2000) and can be explained by the geometry of the system: The galaxy’s disc is oriented so that we see the underside of the disc. The emission from the northwestern halo behind the disc is therefore absorbed by the intervening disc material.

The spectral properties in different regions of the disc are summarised in Table A.1. An example of a disc spectrum (re-

gion 14) is shown in Fig. 6. The visible lines are from O VII (~ 0.57 keV), O VIII (0.65 keV), Fe XVII (0.73–0.83 keV), Ne IX (~ 0.91 keV), Ne X (1.0 keV), Mg XI (~ 1.3 keV), and Si XIII (~ 1.9 keV).

To fit the spectra, we tried several different models, which all contain an absorption model (tbabs, Wilms et al. 2000) for the Galactic foreground N_H of $1.3 \times 10^{20} \text{ cm}^{-2}$ (Dickey & Lockman 1990). Also the abundances were fixed to solar values (see also Sec. 4.4) from Wilms et al. (2000). A simple one-temperature thin thermal plasma model (apec, Smith et al. 2001) did not result in a good fit (i.e. $\chi^2_\nu \leq 1.4$) in any case. Similarly, a power law model did not give good fits. At least three components were necessary for most of the regions: two thin thermal plasmas plus a power law component. The power law was needed to account for the emission above ~ 1 keV and probably results from point sources below the point source detection limit, or incomplete source removal due to too small extraction radii.

The obtained temperatures are quite uniform throughout the disc and vary from 0.1 to 0.3 keV and from 0.3 to 0.8 keV for the soft and the hard component, respectively. The intrinsic luminosity (corrected for Galactic absorption) of the diffuse emission within the inclination corrected optical D_{25} ellipse is $2.4 \times 10^{39} \text{ erg s}^{-1}$ (0.2–10.0 keV), or $8.5 \times 10^{38} \text{ erg s}^{-1}$ (2.0–10 keV). Both values were corrected for the area of cut-out point sources.

The spectra decrease in hardness from the northwest to the southeast parallel to the minor axis, which can easily be seen in the hardness ratio maps (Fig. 5). This is not an effect caused by different temperatures, but by the increasing strength of the

soft spectral component towards the southeast (compared to the hard component), as the optical depth through the halo on the near side of the disc increases.

The regions along the northwestern outflow (regions 9 & 16) as well as the region northeast to that (region 13) allow a lower limit estimate of the absorption through the disc. Here an additional absorption component was required to achieve a good spectral fit. The required column densities range between $\sim 0.5 \times 10^{22} \text{ cm}^{-2}$ and $\sim 0.9 \times 10^{22} \text{ cm}^{-2}$.

In a few cases, the two thermal plasma plus a power law component model did not give the best fit. The southern region on the northeastern end of the disc (region 12) did not require a power law component. It does not cover a spiral arm of NGC 253, thus the contribution from point sources below the detection limit may not be significant. The region furthest to the south in the disc (region 21) was well fit with one thermal plasma and a power law. A second thermal plasma was not required.

We found that spectra are harder in regions which cover spiral arms. The northeastern regions of the disc (regions 11 & 12) are the best example for this. The region which covers the spiral arm (region 11) shows temperatures of $0.18^{+0.05}_{-0.04}$ and $0.58^{+0.16}_{-0.18}$ keV, whereas the region adjacent to the spiral arm (region 12) is significantly cooler with temperatures of 0.07 ± 0.01 and $0.25^{+0.04}_{-0.03}$ keV. The latter spectrum is actually more similar to the typical halo spectrum (see next section).

3.2. Halo diffuse emission

The halo shows emission only below ~ 1 keV. Its projected maximum extent is ~ 9.0 kpc to the northwest, and ~ 6.3 kpc to the southeast, perpendicular to the major axis. The general shape resembles a horn structure. This was already seen with *ROSAT* (e.g. Pietsch et al. 2000), and *Chandra* (e.g. Strickland et al. 2002). In the northwestern halo, the EPIC PN images only show the eastern horn. In the southeastern halo, both the eastern and the western horn are visible in the energies between 0.2 and 0.5 keV. At higher energies, the western horn is not visible.

On smaller scales the halo emission seems not to be uniformly distributed. It shows a filamentary structure, as was seen before in the *ROSAT* data. One notable feature is a brighter knot, which coincides with the nuclear outflow axis in the northwestern halo at a height of about 3.5 kpc above the disc. It is bright in energies between 0.2 and 1.0 keV and appears yellow in the false-colour image (Fig. 3). We checked whether any of the detected structures coincide with chip gaps of the detector, and could therefore be artificial, but no correlation was found.

The spectral properties in different regions in the halo are summarised in Table A.1. To fit the spectra, we applied the same approach as for the disc. Again, simple models cannot describe the spectra. A model with two thin thermal plasmas gave a good fit in all regions in the halo. Unlike in the disc, no power law component was necessary in addition to the thermal components.

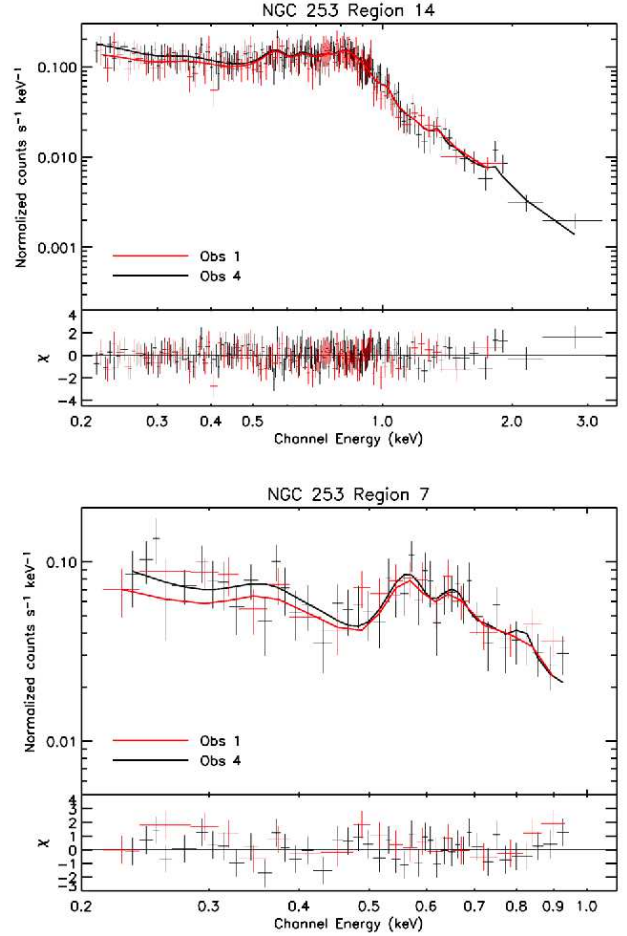


Fig. 6. Representative spectra of a region in the disc (*top*, region 14) and of a region in the halo (*bottom*, region 7). The red and the black data points and model fits are from observations 1 and 4, respectively (see Table 1). The lower panel shows the residuals of the fits.

The southeastern halo is softer than the northwestern halo, which results in redder colours in the southeastern halo in the EPIC PN false-colour image (Fig. 3), and also in lower values in HR1. A fit to the spectrum of the whole northwestern halo gave temperatures of 0.10 ± 0.01 and $0.33^{+0.02}_{-0.01}$ keV. The spectrum in the southeastern halo is similar, with temperatures of 0.09 ± 0.02 and $0.29^{+0.03}_{-0.04}$ keV. The difference in hardness is because the two plasma components contribute different amounts. Compared to the normalisation of the hotter plasma, the normalisation of the cooler plasma is about 1.5 times stronger in the southeastern halo, with respect to the northwestern halo.

The good statistics of the EPIC PN data allowed a further subdivision of the halo into smaller regions. A representative example (region 7) of one of these halo spectra is shown in Fig. 6. The oxygen lines at 0.57 keV (O VII) and 0.65 keV (O VIII) are prominent. Also visible is the iron line at ~ 0.8 keV (Fe XVII).

The halo is not uniform in its spectral properties on smaller scales. The northwestern halo is softer in the east than in the west, while the southeastern halo is softer further away from

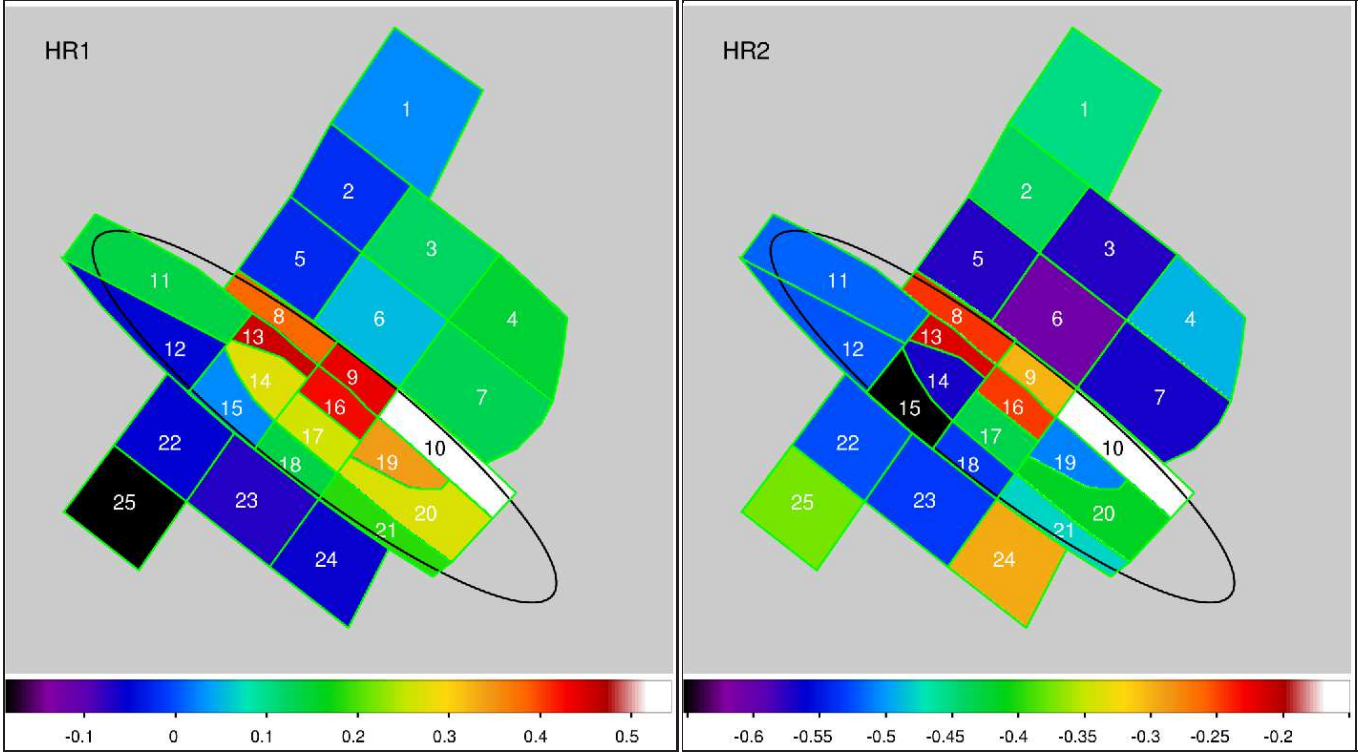


Fig. 5. Hardness ratio maps: The map was binned to the same regions as in Fig. 4. The higher the index, the harder the spectrum. The background colour corresponds to an artificially set value. We also show the inclination corrected optical D_{25} ellipse. (left): $HR1 = (B_2 - B_1) / (B_2 + B_1)$, where B_1 and B_2 are the count rates in the energy bands 0.2–0.5 keV and 0.5–1.0 keV, respectively. (right): $HR2 = (B_3 - B_2) / (B_3 + B_2)$, where B_2 and B_3 are the count rates in the energy bands 0.5–1.0 keV and 1.0–2.0 keV, respectively.

the disc (see HR1 map in Fig. 5). Additionally the emission hardens along the direction of the northwestern outflow (regions 3 & 6). However, the significance of this difference is only 1.9σ .

The total intrinsic luminosity for the diffuse emission, corrected for the area of the removed point sources, in the northwestern halo is $8.4 \times 10^{38} \text{ erg s}^{-1}$ (0.2–1.5 keV), compared to $2.1 \times 10^{38} \text{ erg s}^{-1}$ in the southeastern halo. To calculate electron densities, we assumed a volume for the emitting region. We modeled the northwestern halo with a cylinder with a radius of 4.3 kpc and a height of 4.2 kpc, plus a cylindrical segment with a height of 4.2 kpc, a radius of 4.3 kpc and a width in the southeast-northwest direction of 3.0 kpc (to model region 1). This gives a volume of 298 kpc^3 or $8.7 \times 10^{66} \text{ cm}^3$. For the southeastern halo we assumed a cylinder with a radius of 3.5 kpc and a height of 2.0 kpc, plus a cylindrical segment with a height of 2.0 kpc, a radius of 3.5 kpc and a width in the southeast-northwest direction of 3.0 kpc (region 25), resulting in a volume of 113 kpc^3 or $3.3 \times 10^{66} \text{ cm}^3$. To calculate densities and the total mass in the emission regions, we corrected the volumes for the cut-out point sources. Using the emission measure of the fit (cf. the documentation of the *apec* model in XSPEC), the resulting densities are $3.2 \eta^{-0.5} \times 10^{-3} \text{ cm}^{-3}$ and $4.7 \eta^{-0.5} \times 10^{-3} \text{ cm}^{-3}$ for the northwestern and southeastern halo, respectively. η is the volume filling factor ($\eta \leq 1$). With solar abundances from Wilms et al. (2000), this implies

total masses of $3.3 \eta^{-0.5} \times 10^7 M_{\odot}$ and $1.8 \eta^{-0.5} \times 10^7 M_{\odot}$ for the northwestern and southeastern halo, respectively.

4. Discussion

4.1. The extent of the diffuse emission of NGC 253

Extended emission from the soft northwestern halo was first reported from *Einstein* observations (Fabbiano 1988). Later, observations with *ROSAT* also discovered the southeastern halo in X-rays (e.g. Pietsch et al. 2000). The *ROSAT* images in the soft band trace the emission in the outer halo to projected distances of up to 9 kpc, both in the northwest and the southeast direction. With *XMM-Newton*, the emission is detected out to 9.0 kpc to the northwest and 6.3 kpc to the southeast. This difference in the southeastern halo can be explained by the high *ROSAT* sensitivity extending down to 0.1 keV. The useful *XMM-Newton* EPIC PN range is limited to 0.2 keV. This makes a big difference as there are many strong lines from O IV, Ne VIII, Mg IX, Mg X, Si IX, and Si X in the energy band between 0.1 and 0.2 keV. For a thermal plasma at a temperature of ~ 0.1 keV, these lines are even stronger than the O VII and O VIII lines, and about 60% of the total flux in the energy band from 0.1 to 2.0 keV originates from lines below 0.2 keV. The southeastern halo shows softer emission than the northwestern halo, therefore, the effect is strongest in the southeastern halo.

Also in the disc the extent of the emission is different. The *ROSAT* images trace the soft emission ~ 6.8 kpc towards the

northeast and ~ 5.3 kpc towards the southwest. With *XMM-Newton*, the disc emission has an extent of ~ 7.2 kpc and ~ 6.3 kpc to the northeast and southwest, respectively. The disc spectra are harder than the halo spectra, and therefore the higher *XMM-Newton* sensitivity at energies > 0.4 keV comes into play.

4.2. Is the diffuse emission in the disc really from hot interstellar gas?

The cumulative emission of a large population of weak stellar-type X-ray sources can mimic the characteristics of a hot interstellar gas component. This was first discovered in the Milky Way's ridge X-ray emission (e.g. Revnivtsev et al. 2006), who found evidence that the bulk of the Galactic ridge X-ray emission is composed of weak X-ray sources, mostly cataclysmic variables and coronally active stars in binary systems, with a luminosity of most of these sources of less than 10^{31} erg s $^{-1}$. Also in other galaxies, Revnivtsev et al. (2007) found that the apparently diffuse emission is consistent with the emission from an old stellar population like in the Milky Way.

Can this also explain the extended X-ray emission in the disc of NGC 253? Following the method by Revnivtsev et al. (2007), we used K-band observations, to infer the emissivity of the diffuse X-ray component per unit stellar mass. We derived the near-infrared luminosity and stellar mass of NGC 253, using the total K-band magnitude of 3.772 (Jarrett et al. 2003), the distance modulus of 27.06, corrected for interstellar extinction of 0.007 (Schlegel et al. 1998), and the colour-dependent K-band mass-to-light ratio from (Bell & de Jong 2001, $\log(M_*/L_K) = -0.692 + 0.652 \times (B - V)$), with $(B - V) = -0.16$ (Comerón et al. 2003). This yielded a total K-band luminosity $L_K = 1.6 \times 10^{11} L_\odot$ and a total stellar mass $M_* = 2.6 \times 10^{10} M_\odot$. With a X-ray luminosity of NGC 253 of 2.0×10^{39} erg s $^{-1}$ (0.5–10 keV), the emissivity of the diffuse X-ray component per unit stellar mass then resulted in

$$\frac{L_{0.5-10 \text{ keV}}}{M_*} = 7.6^{+0.9}_{-0.3} (\pm 2.3) \times 10^{28} \text{ erg s}^{-1} M_\odot^{-1}.$$

The errors are statistical errors on the measured X-ray flux. Additionally, we assumed an uncertainty of $\sim 30\%$ (given in parentheses), which might be associated with the L_K to M_* conversion (Bell et al. 2003). The emissivity of NGC 253 should only be considered a lower limit. We cut out a quite large region in the centre of NGC 253 and corrected for this by filling the hole with the average flux of the disc. Therefore, the obtained X-ray luminosity as well as the emissivity are probably too small.

From the luminosity and other properties of the Galactic ridge X-ray emission (e.g. Revnivtsev et al. 2006) and from direct measurements of the luminosity function of sources in the solar neighbourhood (Sazonov et al. 2006), the combined 0.5–10 keV emissivity of cataclysmic variables and coronally active stars has been estimated as $L_X/M_* \sim 1.2 \pm 0.3 \times 10^{28}$ erg s $^{-1} M_\odot^{-1}$. The value derived for NGC 253 is larger than the value for the Milky Way, indicating the presence of a hot gaseous component.

An even stronger argument is the following: if the diffuse X-ray emission is produced by an old stellar population, then their morphologies should be similar. A comparison of the X-ray emission with the 2MASS K-band image (Jarrett et al. 2003) is shown in Fig. 7. We found that the X-ray morphology does not match the K-band morphology, therefore the diffuse emission is indeed not simply due to an old stellar population, but has to have a truly diffuse component.

4.3. Spectral fits and variations in the halo

As it was mentioned already in earlier publications, there is an ambiguity in the spectral fits between a pure multi-temperature thermal plasma model and a combination of thermal plasmas plus a power law component (e.g. Dahlem et al. 2000; Strickland et al. 2002). This ambiguity in the halo emission still exists with the *XMM-Newton* data. Fits to the halo spectra with a thermal plasma plus a power law model (see Table A.2) resulted in similar χ^2_ν , as for a multi-temperature thermal plasma model. A power law component from point sources could be excluded, since we were careful to remove any point source contribution. Another source for non-thermal emission could be synchrotron emission from cosmic ray electrons that are advected with the superwind or are accelerated locally in internal wind shocks. A comparison of the X-ray emission to the 330 MHz and 1.4 GHz radio emission (Carilli et al. 1992) showed that the radio emission is more extended, and does not show the horn structure that we see in X-rays. Because of this inequality, we prefer the multi-temperature thermal plasma model for the X-ray halo emission at the moment. A currently ongoing analysis with non-equilibrium models (e.g. Breitschwerdt & Schmutzler 1999) might also be able to explain the observations.

The northwestern halo shows significant hardness variations in HR1, as opposed to the findings by Strickland et al. (2002). We checked if this can be caused by a different energy band selection, but the result is independent whether we use the bands from Strickland et al. (2002) (0.3–0.6 keV and 0.6–1.0 keV) or our own. These hardness variations might also be a sign of non-equilibrium ionisation (NEI) X-ray emission.

4.4. Temperatures, abundances and column densities

The X-ray emission from NGC 253 has been observed before with several other X-ray observatories. Especially the early observatories did not allow to separate the point sources from the diffuse emission since the point spread function was quite large. Hence, only a combined fit of the emission from the halo, the disc, and the nuclear region was possible. Temperatures of multi-temperature models ranged between 0.1 and 0.3 keV for the low, and between 0.6 and 0.7 keV for the high temperature component (Dahlem et al. 1998; Weaver et al. 2000; Dahlem et al. 2000). Reported abundances were mostly highly subsolar and therefore unphysical for a supposedly metal enriched starburst galaxy plasma.

Only the X-ray observatories like *XMM-Newton*, *Chandra*, and to some degree *ROSAT* allow us to separate the halo from

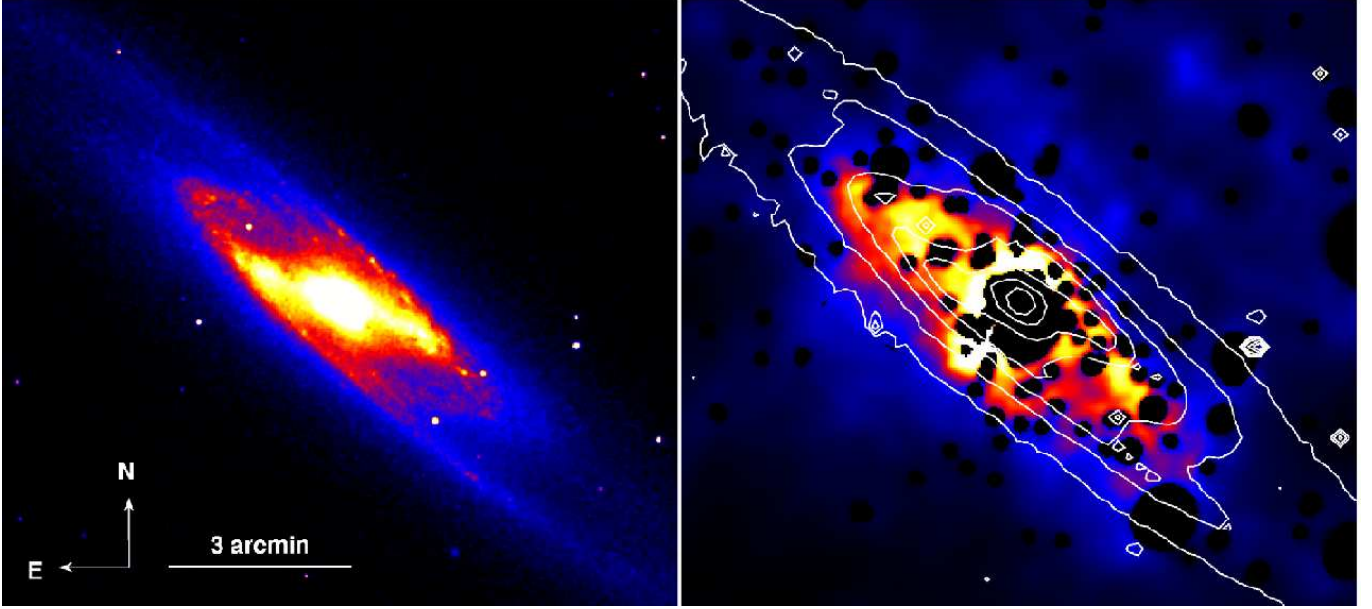


Fig. 7. Comparison between the K-band (left, 2MASS, Jarrett et al. 2003) and X-ray (right) morphology. The white contours overplotted on the X-ray image represent the K-band brightness levels. Both images are on a linear colour scale, and on the same spatial scale as indicated in the K-band image.

the disc emission and to remove contribution by point sources via a spatial selection. From *ROSAT* data, Pietsch et al. (2000) inferred a foreground absorbed two-temperature thermal model with temperatures of 0.13 and 0.62 keV for the northwestern halo emission. No highly subsolar abundances were required. The disc emission could be explained by a 0.7 keV thermal plasma and an additional thermal plasma ($kT=0.2$ keV) in front of the disc coming from a coronal component.

The first *XMM-Newton* results by Pietsch et al. (2001) required a two-component model for the disc emission with temperatures of 0.13 and 0.4 keV plus residual harder emission, possibly from unresolved point sources. For the nuclear region three temperatures were needed (0.6, 0.9, and 6 keV). Both models used solar abundances. No analysis of the halo emission was presented in their paper.

The best spatial resolution is provided by the *Chandra* observatory. Results on the diffuse disc and halo emission were first published by Strickland et al. (2002). For the halo emission they needed a multi-temperature model (apec) with at least two temperatures of 0.24 and 0.71 keV (the latter with quite large errors) and with a foreground absorption of $5.3 \times 10^{20} \text{ cm}^{-2}$. A power law ($\Gamma = 3.3$) plus a thermal plasma ($kT=0.24$ keV) gave a similarly good fit. A combination of other thermal models (mekal) or non-equilibrium models (vnei) did not result in better fits. The diffuse emission from the disc was fitted with the same models, however, the temperatures were lower than in the halo, with 0.17 and 0.56 keV, respectively. The foreground absorption yields $4.7 \times 10^{20} \text{ cm}^{-2}$. In all cases unphysically sub-solar abundances had to be assumed.

The temperature values for the halo emission, as found by our analysis, are lower than the ones from previous observations. Our soft component is about 0.10 keV, which is still compatible with the *ROSAT* results. However, the hard component

is only ~ 0.32 keV for the northwestern halo and ~ 0.29 keV for the southeastern halo. A higher temperature was not necessary in any of our fits. A possible explanation could be the way the spectra were background subtracted. We used a sophisticated method (see App. C) that uses the local background at the border of the field of view, where no emission from NGC 253 is expected, while other authors used e.g. blank-sky observations (Strickland et al. 2002). Using a background from different times and different fields on the sky can lead to systematic effects in the background subtraction. A background region with a higher contribution of the local bubble could, for example, lead to an over-correction, especially at very soft energies (<0.5 keV).

In the disc we found temperatures between 0.1 and 0.3 keV and between 0.3 and 0.8 keV, for the soft and the hard component, respectively. This is consistent with earlier results.

We also tried to constrain the metal abundances in our fits. However the errors on the obtained values are so large, that we are not able to give well constrained abundances (northwestern halo: $Z = 0.3^{+4.7}_{-0.2} Z_{\odot}$, southeastern halo: $Z = 0.4^{+4.6}_{-0.3} Z_{\odot}$, disc: $Z = 1.0^{+0.9}_{-0.7} Z_{\odot}$). Since we do not expect highly subsolar abundances in an environment which is enriched with metals from the starburst via the superwind and galactic fountains, we fixed the abundances in our analysis to solar. This is very well consistent with the above values. A reason for the low abundances, found with different instruments, could be that due to a lower spatial resolution and/or sensitivity more point sources contribute to the final spectrum, increasing the continuum flux. The ratio of line emission to continuum flux is therefore decreased, which mimics the spectral shape of a plasma with low metal abundances. A similar effect can be achieved when a NEI spectrum is fitted with CIE models. Also, a too

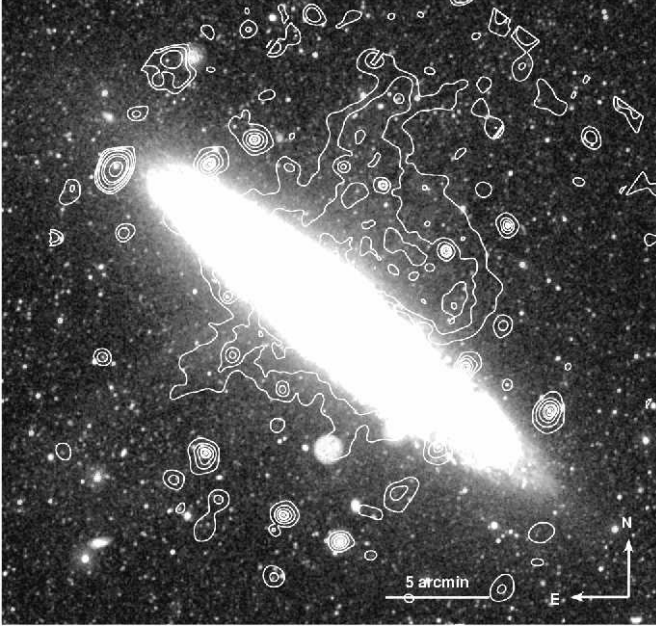


Fig. 8. Two-colour UV image of NGC 253 with NUV (175–280 nm) in yellow and FUV (135–175 nm) in blue. The intensity was rescaled to emphasise the faint, diffuse emission. Overplotted are the 0.2–0.5 keV X-ray contours.

simplistic model could be the reason, combining regions with different temperatures.

In the disc, three of the regions required an extra absorption component in the spectral model. The additional column densities range between $0.5 \times 10^{22} \text{ cm}^{-2}$ and $0.9 \times 10^{22} \text{ cm}^{-2}$. Direct radio measurements of the HI column density showed lower values than we derived from the X-ray data. An interpolation of the HI maps by Puche et al. (1991) and Koribalski et al. (1995) resulted in ~ 2.4 , 3.9 , and $3.4 \times 10^{21} \text{ cm}^{-2}$ for regions 9, 13, and 16, respectively. However, the HI value for the region including the nucleus of NGC 253 (region 16) is affected by HI absorption, so the resulting column density can only be considered as a lower limit. Additional absorption is expected from molecular hydrogen. Mauersberger et al. (1995) derived the H_2 column density in the direction of the nucleus of NGC 253 to $3.7 \times 10^{23} \text{ cm}^{-2}$. Taking this value as an upper limit for the column density in the disc regions around the nucleus, the column densities derived from X-ray spectra are within the limits from radio observations.

4.5. X-ray versus UV morphology

Fig. 8 shows the X-ray contours from the energy band 0.2–0.5 keV overplotted on a two-colour UV image, taken with the GALEX observatory (Galaxy Evolution Explorer, a UV space telescope) on 2003 October 13. For the northwestern halo there is quite a good agreement between the FUV and X-ray emission regions. The FUV emission traces the western horn to a distance of ~ 7.5 kpc above the disc, as well as the broad base emission in soft X-rays quite well. In the southeastern halo, again, the UV and the soft X-ray emission show the western

horn structure, where the UV horn extends to about 7 kpc away from the disc. However, the FUV horn is slightly offset by ~ 700 pc to the northeast with respect to the X-ray horn. Images obtained with the Optical Monitor onboard *XMM-Newton* are not sensitive enough to show the extraplanar UV emission.

Hoopes et al. (2005) proposed the following model for the origin of the UV emission: Since the UV luminosities are too high to be produced by continuum and line emission from photoionized or shock-heated gas, the UV emission could be explained by dust in the outflow that scatters the stellar continuum from the starburst into our line of sight. They also found that the UV halo emission, as seen with GALEX, correlates with the $\text{H}\alpha$ emission, which could originate from gas that is photoionized by UV photons from the starburst. The UV and $\text{H}\alpha$ emission would originate in the same cold regions in the halo.

How does the warm gas that is responsible for the $\text{H}\alpha$ and UV emission get out into the halo? There are two possibilities: either it has already been there from the beginning in the form of a cold and maybe clumpy halo component, or it was transported by the superwind and galactic fountains from the disc out into the halo.

There are models, where it is possible to drag up clouds of cold gas into the halo (e.g. model 3 of Strickland et al. 2002). In a sheet surrounding these clouds, X-ray emission could be produced by shocks or in conductive or turbulent mixing interfaces on the cloud surface. This model would also account for the non-uniformity of the X-ray emission as seen in the *XMM-Newton* images (Fig. 1 and 3). However, the model cannot explain the displacement of the UV emission in the southeastern halo, since in the model the clouds are located within or at the inner border of the superwind.

Could the dust even survive this transport from the disc into the halo embedded in a hot plasma environment? Draine & Salpeter (1979) give the sputtering time for a spherical dust grain of radius a embedded in a plasma of hydrogen with temperatures between 10^6 and 10^9 K and the density n_{H} as

$$t_{\text{sput}} \sim 10^6 \left(\frac{a}{\mu\text{m}} \right) \left(\frac{n_{\text{H}}}{\text{cm}^{-3}} \right)^{-1} \text{ yr.} \quad (1)$$

For n_{H} between $2.5 \times 10^{-2} \text{ cm}^{-3}$ in the outflow close to the centre (Bauer et al. 2007) and $3.2 \times 10^{-3} \text{ cm}^{-3}$ out in the northwestern halo, and a grain size of $a=0.1 \mu\text{m}$, t_{sput} varies between 4.0 and 31 Myr. So to reach a height above the disc of 7.5 kpc in less than 31 Myr, an average velocity of at least 240 km/s is required. This is well compatible with measurements of outflow velocities in different wavelengths, that range from 260 km/s (Na D absorption, Heckman et al. 2000) to about 400–600 km/s ($\text{H}\alpha$, N II, S II, and O II emission, Ulrich 1978; Demoulin & Burbidge 1970). Therefore it is quite possible that the dust survives the transport from the disc out into the halo.

Another model to explain the UV and X-ray morphology (e.g. model 5 of Strickland et al. 2002) requires a thick disc component, through which the superwind emerges into the halo. On the contact surface between the hot superwind fluid and the cold thick disc material we get a heated layer through

shocks and turbulent mixing where the X-rays are produced, surrounded on the outside by a colder layer where the UV emission originates. The thick disc component was originally created by lifting material up from the disc through the star formation activity (simulations by Rosen & Bregman 1995). This model would easily explain the UV displacement from the X-rays, however we would only get a hollow cone with X-ray emission. The latter is not what we see in the *XMM-Newton* observations. Though a mix of both models would be able to explain the observed morphology.

The magnetohydrodynamics ISM simulations of de Avillez & Breitschwerdt (2005) also shows a clumpy halo structure, characterized by turbulent mixing layers, which could explain the UV and X-ray filamentary structure. In some regions, the magnetic field forms loops surrounded by shells which may exhibit enhanced UV emission.

5. Summary

We have characterised the diffuse emission in NGC 253. The disc extends 13.6 kpc along the major axis and shows emission between 0.2 and 10 keV. The spectrum could be modelled with two thermal plasmas ($T_{\text{cold}} = 0.1 - 0.3$ keV and $T_{\text{hot}} = 0.3 - 0.8$ keV) with solar abundances plus a power law component and galactic foreground absorption. The power law component may indicate an unresolved contribution from X-ray binaries in the disc. The total luminosity of the diffuse emission in the disc is 2.4×10^{39} erg s⁻¹ (0.2-10.0 keV). We found clear evidence for hot plasma in the disc. The diffuse emission does not originate completely from an old stellar population.

The halo resembles a horn structure which reaches out to a projected height of ~ 9 kpc perpendicular to the disc. The halo emission on smaller scales seems not to be uniformly distributed, but shows a filamentary structure. The southeastern halo is softer than the northwestern halo. To model the spectra in the halo we needed two thermal plasmas ($T_{\text{cold}} \sim 0.1$ keV and $T_{\text{hot}} \sim 0.3$ keV) with solar abundances plus galactic foreground absorption. The total luminosity of the diffuse emission is 8.4×10^{38} erg s⁻¹ and 2.1×10^{38} erg s⁻¹ (0.2-1.5 keV) in the northwestern and southeastern halo, respectively. Densities computed to $3.2 \eta^{-0.5} \times 10^{-3}$ cm⁻³ and $4.7 \eta^{-0.5} \times 10^{-3}$ cm⁻³, with the volume filling factor η . With solar abundances this implies total masses of $3.3 \eta^{-0.5} \times 10^7 M_{\odot}$ and $1.8 \eta^{-0.5} \times 10^7 M_{\odot}$ for the northwestern and southeastern halo, respectively.

A comparison between X-ray and UV emission showed that both originate from the same regions. The UV emission is more extended in the southeastern halo, where it seems to form a shell around the X-ray emission.

Acknowledgements. The *XMM-Newton* project is supported by the Bundesministerium für Wirtschaft und Technologie/Deutsches Zentrum für Luft- und Raumfahrt (BMWi/DLR, FKZ 50 OX 0001), and the Max-Planck Society. This research has made use of the NASA/IPAC Extragalactic Database (NED) which is operated by the Jet Propulsion Laboratory, California Institute of Technology, under contract with the National Aeronautics and Space Administration. This research has made use of the SIMBAD database, operated at CDS, Strasbourg, France. The GALEX data presented in this paper were obtained from the Multimission Archive at the Space Telescope

Science Institute (MAST). STScI is operated by the Association of Universities for Research in Astronomy, Inc., under NASA contract NAS5-26555. Support for MAST for non-HST data is provided by the NASA Office of Space Science via grant NAG5-7584 and by other grants and contracts. MB acknowledges support from the BMWI/DLR, FKZ 50 OR 0405.

References

- Bauer, M., Pietsch, W., Trinchieri, G., et al. 2007, *A&A*, 467, 979
- Bell, E. F. & de Jong, R. S. 2001, *ApJ*, 550, 212
- Bell, E. F., McIntosh, D. H., Katz, N., & Weinberg, M. D. 2003, *ApJS*, 149, 289
- Breitschwerdt, D. & Schmutzler, T. 1999, *A&A*, 347, 650
- Cappi, M., Persic, M., Bassani, L., et al. 1999, *A&A*, 350, 777
- Carilli, C. L., Holdaway, M. A., Ho, P. T. P., & de Pree, C. G. 1992, *ApJ*, 399, L59
- Comerón, F., Gómez, A. E., & Torra, J. 2003, *A&A*, 400, 137
- Dahlem, M., Parmar, A., Oosterbroek, T., et al. 2000, *ApJ*, 538, 555
- Dahlem, M., Weaver, K. A., & Heckman, T. M. 1998, *ApJS*, 118, 401
- de Avillez, M. A. & Breitschwerdt, D. 2005, *A&A*, 436, 585
- Demoulin, M. H. & Burbidge, E. M. 1970, *ApJ*, 159, 799
- den Herder, J. W., Brinkman, A. C., Kahn, S. M., et al. 2001, *A&A*, 365, L7
- Dickey, J. M. & Lockman, F. J. 1990, *ARA&A*, 28, 215
- Draine, B. T. & Salpeter, E. E. 1979, *ApJ*, 231, 77
- Fabbiano, G. 1988, *ApJ*, 330, 672
- Fabbiano, G. & Trinchieri, G. 1984, *ApJ*, 286, 491
- Freeman, P. E., Kashyap, V., Rosner, R., & Lamb, D. Q. 2002, *ApJS*, 138, 185
- Freyberg, M. J., Briel, U. G., Dennerl, K., et al. 2004, in *X-Ray and Gamma-Ray Instrumentation for Astronomy XIII*. Edited by Flanagan, Kathryn A.; Siegmund, Oswald H. W. Proceedings of the SPIE, Volume 5165., ed. K. A. Flanagan & O. H. W. Siegmund, 112–122
- Gehrels, N. 1986, *ApJ*, 303, 336
- Heckman, T. M., Lehnert, M. D., Strickland, D. K., & Armus, L. 2000, *ApJS*, 129, 493
- Hoopes, C. G., Heckman, T. M., Strickland, D. K., et al. 2005, *ApJ*, 619, L99
- Jansen, F., Lumb, D., Altieri, B., et al. 2001, *A&A*, 365, L1
- Jarrett, T. H., Chester, T., Cutri, R., Schneider, S. E., & Huchra, J. P. 2003, *AJ*, 125, 525
- Koribalski, B., Whiteoak, J. B., & Houghton, S. 1995, *Publications of the Astronomical Society of Australia*, 12, 20
- Mason, K. O., Breeveld, A., Much, R., et al. 2001, *A&A*, 365, L36
- Mauersberger, R., Henkel, C., & Chin, Y.-N. 1995, *A&A*, 294, 23
- Monet, D. G., Levine, S. E., Canzian, B., et al. 2003, *AJ*, 125, 984
- Pence, W. D. 1980, *ApJ*, 239, 54
- Pietsch, W. 1992, in *Physics of Nearby Galaxies: Nature or Nurture?*, ed. T. X. Thuan, C. Balkowski, & J. Tran Thanh

- van, 67
- Pietsch, W., Roberts, T. P., Sako, M., et al. 2001, *A&A*, 365, L174
- Pietsch, W., Vogler, A., Klein, U., & Zinnecker, H. 2000, *A&A*, 360, 24
- Ptak, A., Serlemitsos, P., Yaqoob, T., Mushotzky, R., & Tsuru, T. 1997, *AJ*, 113, 1286
- Puche, D., Carignan, C., & van Gorkom, J. H. 1991, *AJ*, 101, 456
- Read, A. M., Ponman, T. J., & Strickland, D. K. 1997, *MNRAS*, 286, 626
- Revnivtsev, M., Churazov, E., Sazonov, S., Forman, W., & Jones, C. 2007, *ArXiv Astrophysics e-prints*
- Revnivtsev, M., Sazonov, S., Gilfanov, M., Churazov, E., & Sunyaev, R. 2006, *A&A*, 452, 169
- Rosen, A. & Bregman, J. N. 1995, *ApJ*, 440, 634
- Sazonov, S., Revnivtsev, M., Gilfanov, M., Churazov, E., & Sunyaev, R. 2006, *A&A*, 450, 117
- Schlegel, D. J., Finkbeiner, D. P., & Davis, M. 1998, *ApJ*, 500, 525
- Smith, R. K., Brickhouse, N. S., Liedahl, D. A., & Raymond, J. C. 2001, *ApJ*, 556, L91
- Snowden, S. L., Collier, M. R., & Kuntz, K. D. 2004, *ApJ*, 610, 1182
- Strickland, D. K., Heckman, T. M., Colbert, E. J. M., Hoopes, C. G., & Weaver, K. A. 2004a, *ApJS*, 151, 193
- Strickland, D. K., Heckman, T. M., Colbert, E. J. M., Hoopes, C. G., & Weaver, K. A. 2004b, *ApJ*, 606, 829
- Strickland, D. K., Heckman, T. M., Weaver, K. A., Hoopes, C. G., & Dahlem, M. 2002, *ApJ*, 568, 689
- Strüder, L., Briel, U., Dennerl, K., et al. 2001, *A&A*, 365, L18
- Turner, M. J. L., Abbey, A., Arnaud, M., et al. 2001, *A&A*, 365, L27
- Ulrich, M.-H. 1978, *ApJ*, 219, 424
- Vogler, A. & Pietsch, W. 1999, *A&A*, 342, 101
- Weaver, K. A., Heckman, T. M., & Dahlem, M. 2000, *ApJ*, 534, 684
- Weaver, K. A., Heckman, T. M., Strickland, D. K., & Dahlem, M. 2002, *ApJ*, 576, L19
- Wilms, J., Allen, A., & McCray, R. 2000, *ApJ*, 542, 914

Appendix A: Spectral fits

Table A.1. Spectral fits (multi-temperature thermal plasma, plus power law component in the disc) and hardness ratios in the extraction regions.

Region	χ^2_ν (χ^2/ν)	kT (keV)	norm (10^{-5})	N_H (10^{22} cm^{-2})	kT (keV)	norm (10^{-5})	Γ	norm (10^{-5})	HR1	HR2
1	1.0 (21.1/21.0)	$0.10^{+0.02}_{-0.02}$	$19.4^{+8.5}_{-8.3}$...	$0.35^{+0.06}_{-0.05}$	$5.6^{+1.6}_{-1.5}$	0.03 ± 0.04	-0.45 ± 0.03
2	0.8 (14.6/18.0)	$0.10^{+0.03}_{-0.02}$	$8.3^{+4.2}_{-3.8}$...	$0.32^{+0.06}_{-0.05}$	$3.0^{+1.0}_{-0.9}$	-0.02 ± 0.04	-0.44 ± 0.04
3	0.9 (35.3/39.0)	$0.09^{+0.01}_{-0.02}$	$11.6^{+6.0}_{-5.0}$...	$0.34^{+0.05}_{-0.03}$	$4.6^{+0.9}_{-0.9}$	0.12 ± 0.03	-0.57 ± 0.02
4	0.7 (16.5/25.0)	$0.11^{+0.04}_{-0.03}$	$5.7^{+3.9}_{-2.9}$...	$0.33^{+0.07}_{-0.04}$	$3.3^{+0.9}_{-0.9}$	0.15 ± 0.04	-0.49 ± 0.03
5	0.8 (31.1/41.0)	$0.10^{+0.02}_{-0.02}$	$11.5^{+4.1}_{-2.7}$...	$0.30^{+0.04}_{-0.04}$	$3.4^{+0.6}_{-0.6}$	-0.02 ± 0.03	-0.57 ± 0.02
6	0.9 (82.5/90.0)	$0.10^{+0.01}_{-0.01}$	$15.4^{+3.3}_{-4.1}$...	$0.32^{+0.03}_{-0.02}$	$6.0^{+0.9}_{-0.8}$	0.05 ± 0.02	-0.61 ± 0.03
7	0.9 (52.0/59.0)	$0.11^{+0.02}_{-0.03}$	$8.2^{+3.7}_{-2.8}$...	$0.31^{+0.03}_{-0.03}$	$5.0^{+0.9}_{-1.1}$	0.13 ± 0.03	-0.57 ± 0.02
8	0.38 ± 0.04	-0.24 ± 0.04
9	0.8 (36.4/47.0)	$0.17^{+0.08}_{-0.07}$	$1.1^{+1.2}_{-0.9}$	$0.496^{+0.391}_{-0.169}$	$0.32^{+0.08}_{-0.07}$	$9.2^{+4.7}_{-4.9}$	$1.12^{+0.54}_{-0.43}$	$0.9^{+0.4}_{-0.6}$	0.44 ± 0.04	-0.30 ± 0.03
10	0.55 ± 0.06	-0.15 ± 0.04
11	0.6 (47.0/78.0)	$0.18^{+0.05}_{-0.04}$	$3.4^{+1.4}_{-1.3}$...	$0.58^{+0.16}_{-0.18}$	$1.9^{+0.8}_{-0.8}$	$2.54^{+0.53}_{-0.76}$	$1.2^{+0.8}_{-1.2}$	0.14 ± 0.03	-0.52 ± 0.02
12	1.4 (43.3/32.0)	$0.07^{+0.01}_{-0.01}$	$17.2^{+12.0}_{-9.6}$...	$0.25^{+0.04}_{-0.03}$	$2.7^{+0.6}_{-0.6}$	-0.05 ± 0.04	-0.52 ± 0.03
13	0.8 (41.1/53.0)	$0.30^{+0.07}_{-0.06}$	$1.9^{+0.7}_{-1.0}$	$0.892^{+1.095}_{-0.408}$	$0.77^{+0.91}_{-0.45}$	$4.2^{+4.8}_{-3.8}$	$0.67^{+0.78}_{-0.67}$	$0.7^{+0.7}_{-0.6}$	0.46 ± 0.04	-0.22 ± 0.04
14	0.5 (149.0/275.0)	$0.20^{+0.05}_{-0.05}$	$4.3^{+1.0}_{-1.6}$...	$0.59^{+0.06}_{-0.05}$	$5.7^{+1.1}_{-1.6}$	$2.12^{+0.23}_{-0.31}$	$2.2^{+0.6}_{-0.5}$	0.27 ± 0.02	-0.57 ± 0.02
15	0.7 (80.2/116.0)	$0.20^{+0.05}_{-0.06}$	$2.8^{+0.9}_{-1.3}$...	$0.59^{+0.15}_{-0.15}$	$1.6^{+0.9}_{-1.4}$	$3.13^{+0.31}_{-0.32}$	$1.0^{+0.5}_{-0.4}$	0.03 ± 0.02	-0.65 ± 0.02
16 (NW outflow)	0.8 (126.1/150.0)	$0.25^{+0.08}_{-0.07}$	$1.8^{+2.1}_{-1.0}$	$0.542^{+0.239}_{-0.179}$	$0.59^{+0.11}_{-0.12}$	$9.1^{+3.7}_{-5.2}$	$1.38^{+0.19}_{-0.18}$	$2.0^{+0.4}_{-0.5}$	0.43 ± 0.02	-0.24 ± 0.02
17 (Centre)	0.8 (187.1/249.0)	$0.24^{+0.06}_{-0.04}$	$2.6^{+1.6}_{-1.4}$...	$0.58^{+0.08}_{-0.12}$	$2.8^{+1.2}_{-1.1}$	$1.73^{+0.16}_{-0.11}$	$3.3^{+0.5}_{-0.6}$	0.26 ± 0.02	-0.43 ± 0.02
18 (SE outflow)	0.5 (82.1/152.0)	$0.24^{+0.04}_{-0.04}$	$2.9^{+1.2}_{-1.3}$...	$0.66^{+0.19}_{-0.22}$	$1.2^{+1.0}_{-0.8}$	$2.28^{+0.27}_{-0.33}$	$1.8^{+0.5}_{-0.5}$	0.14 ± 0.02	-0.53 ± 0.02
19	0.7 (84.5/114.0)	$0.19^{+0.05}_{-0.05}$	$2.7^{+0.8}_{-1.0}$...	$0.59^{+0.10}_{-0.11}$	$2.4^{+0.8}_{-0.9}$	$1.09^{+0.55}_{-0.32}$	$1.1^{+0.5}_{-0.8}$	0.34 ± 0.03	-0.51 ± 0.02
20	1.0 (73.7/77.0)	$0.21^{+0.05}_{-0.05}$	$3.0^{+1.1}_{-1.8}$...	$0.57^{+0.16}_{-0.47}$	$1.7^{+0.8}_{-1.6}$	$1.51^{+0.36}_{-0.28}$	$2.2^{+0.7}_{-0.7}$	0.27 ± 0.03	-0.42 ± 0.03
21	0.8 (32.3/39.0)	$0.20^{+0.07}_{-0.07}$	$1.7^{+0.7}_{-1.1}$	$1.39^{+0.64}_{-0.76}$	$2.1^{+0.8}_{-0.7}$	0.19 ± 0.04	-0.48 ± 0.02
22	0.9 (45.3/48.0)	$0.10^{+0.02}_{-0.02}$	$8.9^{+2.3}_{-2.4}$...	$0.32^{+0.06}_{-0.05}$	$1.9^{+0.5}_{-0.8}$	-0.05 ± 0.04	-0.53 ± 0.03
23	0.9 (54.0/62.0)	$0.09^{+0.02}_{-0.01}$	$13.5^{+3.4}_{-3.9}$...	$0.30^{+0.04}_{-0.03}$	$3.1^{+0.8}_{-0.7}$	-0.07 ± 0.03	-0.53 ± 0.03
24	-0.06 ± 0.05	-0.30 ± 0.04
23+24	1.1 (82.5/75.0)	$0.07^{+0.01}_{-0.01}$	$46.7^{+20.6}_{-15.2}$...	$0.26^{+0.03}_{-0.02}$	$6.2^{+1.0}_{-1.0}$	-0.07 ± 0.03	-0.45 ± 0.02
25	0.4 (8.5/20.0)	$0.09^{+0.03}_{-0.03}$	$8.5^{+3.3}_{-4.1}$...	$0.24^{+0.08}_{-0.06}$	$1.3^{+1.2}_{-0.8}$	-0.19 ± 0.05	-0.37 ± 0.04
1...7 (NW halo)	0.8 (209.4/261.0)	$0.10^{+0.01}_{-0.01}$	$97.5^{+11.6}_{-12.4}$...	$0.33^{+0.02}_{-0.01}$	$34.7^{+2.7}_{-3.6}$	0.04 ± 0.01	-0.55 ± 0.01
22...25 (SE halo)	1.1 (82.4/76.0)	$0.09^{+0.02}_{-0.02}$	$34.9^{+9.2}_{-5.8}$...	$0.29^{+0.03}_{-0.04}$	$7.5^{+2.0}_{-1.8}$	-0.08 ± 0.02	-0.46 ± 0.02
2...4	1.0 (97.8/99.0)	$0.10^{+0.01}_{-0.01}$	$26.6^{+8.6}_{-7.8}$...	$0.33^{+0.03}_{-0.03}$	$11.1^{+1.8}_{-1.6}$	0.09 ± 0.02	-0.51 ± 0.02
5...7	0.9 (157.8/168.0)	$0.10^{+0.01}_{-0.01}$	$36.8^{+6.1}_{-7.1}$...	$0.32^{+0.02}_{-0.02}$	$14.8^{+1.7}_{-1.9}$	0.06 ± 0.02	-0.59 ± 0.01
22...24	1.1 (91.1/81.0)	$0.09^{+0.02}_{-0.02}$	$29.0^{+6.7}_{-7.6}$...	$0.29^{+0.03}_{-0.03}$	$6.7^{+1.7}_{-1.4}$	-0.06 ± 0.02	-0.48 ± 0.02

NOTE: All errors are 90% confidence for a number of interesting parameters equal to the number of free parameters in the model (3, 4, 5, 6, 7, or 9 free parameters depending on the model). Thin thermal plasma models are apec, absorption models are tbabs. All models have a fixed foreground absorption of $1.3 \times 10^{20} \text{ cm}^{-2}$. For region 8, 10 and 24 no spectral fit was attempted due to low statistics. The hardness ratios in these regions do give meaningful values though.

Table A.2. Spectral fits in the halo extraction regions with a thin thermal plasma plus power law component, as opposed to a multi-temperature thermal plasma model in Table A.1.

Region	χ^2_ν (χ^2/ν)	kT (keV)	norm (10^{-5})	Γ	norm (10^{-5})
1	1.1 (22.3/21.0)	$0.19^{+0.21}_{-0.19}$	$1.3^{+2.9}_{-1.3}$	$1.90^{+0.64}_{-0.61}$	$5.6^{+1.8}_{-2.0}$
2	0.7 (12.5/18.0)	$0.24^{+0.08}_{-0.06}$	$2.0^{+1.5}_{-1.4}$	$2.48^{+0.60}_{-0.86}$	$1.5^{+0.9}_{-1.0}$
3	1.1 (41.2/39.0)	$0.32^{+0.06}_{-0.04}$	$3.8^{+1.4}_{-1.1}$	$3.09^{+0.34}_{-0.57}$	$0.9^{+0.5}_{-0.7}$
4	1.0 (24.4/25.0)	$0.29^{+0.05}_{-0.05}$	$3.1^{+1.3}_{-1.3}$	$2.87^{+0.56}_{-1.11}$	$0.7^{+0.6}_{-0.7}$
5	0.8 (32.9/41.0)	$0.21^{+0.04}_{-0.04}$	$2.5^{+1.2}_{-1.2}$	$2.60^{+0.43}_{-0.53}$	$1.5^{+0.6}_{-0.5}$
6	0.8 (74.9/90.0)	$0.25^{+0.03}_{-0.03}$	$4.2^{+1.4}_{-1.5}$	$2.41^{+0.30}_{-0.32}$	$2.6^{+0.6}_{-0.7}$
7	0.7 (41.7/59.0)	$0.22^{+0.04}_{-0.04}$	$2.9^{+1.8}_{-1.5}$	$1.74^{+0.47}_{-0.62}$	$3.5^{+1.1}_{-1.5}$
22	0.9 (44.0/48.0)	$0.16^{+0.06}_{-0.05}$	$1.8^{+1.3}_{-1.2}$	$2.40^{+0.64}_{-0.66}$	$1.4^{+0.4}_{-0.4}$
23	0.9 (52.8/62.0)	$0.24^{+0.03}_{-0.03}$	$2.7^{+1.0}_{-0.9}$	$3.25^{+0.35}_{-0.37}$	$0.8^{+0.3}_{-0.3}$
25	0.5 (10.4/20.0)	$0.18^{+0.05}_{-0.05}$	$1.9^{+2.0}_{-1.0}$	$3.80^{+0.66}_{-0.84}$	$0.3^{+0.2}_{-0.3}$
23+24	1.3 (98.6/75.0)	$0.22^{+0.07}_{-0.08}$	$0.9^{+4.7}_{-0.5}$	$2.49^{+0.28}_{-0.35}$	$3.5^{+0.3}_{-1.9}$
1...7 (NW halo)	0.8 (201.6/261.0)	$0.26^{+0.01}_{-0.01}$	$29.1^{+3.9}_{-4.4}$	$2.84^{+0.16}_{-0.16}$	$10.2^{+1.5}_{-1.3}$
22...25 (SE halo)	1.1 (81.2/76.0)	$0.21^{+0.04}_{-0.03}$	$6.2^{+2.6}_{-2.4}$	$3.03^{+0.37}_{-0.43}$	$2.7^{+0.8}_{-0.8}$
2...4	1.0 (101.6/99.0)	$0.28^{+0.04}_{-0.04}$	$7.5^{+2.9}_{-2.5}$	$2.46^{+0.29}_{-0.48}$	$4.5^{+1.4}_{-1.5}$
5...7	0.9 (151.8/168.0)	$0.25^{+0.02}_{-0.02}$	$12.4^{+2.4}_{-2.6}$	$2.65^{+0.23}_{-0.24}$	$4.8^{+1.0}_{-1.1}$
22...24	1.2 (93.9/81.0)	$0.23^{+0.03}_{-0.03}$	$5.7^{+2.0}_{-1.8}$	$3.14^{+0.33}_{-0.37}$	$1.9^{+0.6}_{-0.6}$

NOTE: All errors are 90% confidence for a number of interesting parameters equal to the number of free parameters in the model. Thin thermal plasma models are apec. All models have a fixed foreground absorption of $1.3 \times 10^{20} \text{ cm}^{-2}$.

Appendix B: EPIC PN images

We developed an algorithm to create vignetting corrected and adaptively smoothed EPIC PN images. This procedure is based on the observation itself. Specifically, closed filter observations were not used in addition. In the following we will describe the algorithm step-by-step.

The basis for this procedure is a cleaned event file and an out-of-time event file. This cleaning included screening for high background and also removing bad pixels and bad columns. If we want to use more than one observation, all steps have to be performed for all observations separately, before the products are merged.

We will here concentrate on the creation of three images, which can be combined to a RGB colour image at the end of the procedure. In the following all steps are to be done for all three energy bands, unless stated otherwise.

For the desired energy band, we extracted an image from the event file. This image was then corrected for out-of-time events, via subtraction of an image that was extracted from the out-of-time event file and rescaled with the out-of-time event fraction. Next, we corrected for the detector background (electronic noise, high energy particles) by subtracting the detector background surface brightness from the image. This value was determined from the corners of the detector which are outside of the field of view of the telescope. We here assumed that the detector background is uniform across the whole detector (for energies above ~ 7.2 keV this is no longer a good approximation, see Freyberg et al. 2004).

We created vignetting corrected exposure maps and masks using the SAS-tasks `eexpmap` and `emask`, respectively, which will be used to account for differences in the exposure times in the images, and to mask the images to regions with an acceptable minimum exposure time. Before we could smooth the image adaptively, we had to create a template with smoothing kernels. This template guarantees that images in different energy bands are smoothed with the same kernel size. Therefore we added up the images in the different energy bands. With the task `asmooth`, we created the template using the merged image, the merged mask, and an exposure map.

Now we have all the necessary products to smooth the single images. We smoothed the images in the different energy bands with the smoothing template, the vignetting corrected exposure map, and with the corresponding mask. This step included the vignetting correction via the exposure map, and a masking of the image to a region with an acceptable minimum exposure time.

In a final step we used `ds9` to create the RGB colour image. The resulting images of NGC 253 and a combined RGB colour image of the lowest three energy bands is shown in Fig. 1, 2, and 3.

Appendix C: Background spectra

The conventional way to create a background spectrum is to select a region from the same observation where there is no emission from the source. Additionally, the region should be close to the source. This way, the spectral background should

Table C.1. Rejected CCD rows due to MIPs per time unit in the used observations.

Obs ID	Filter	rejected line counter value
0122320707	Closed	181.7
0125960101	Medium	190.2
0152020101	Thin	141.4
0160362801	Closed	120.4

have the same characteristics as the background at the source region. In NGC 253, a region which suffices the first criterion can be found at the border of the field of view in the southwestern part of the detector. The second criterion, however, is not satisfied. The background region may show a different detector background, and additionally the vignetting is different.

Since we were interested in determining the characteristics of emission with low surface brightness, that extends over a large region, where the background is (probably) the dominant component, we needed a very accurate estimate of the background. Given the very soft nature of the emission, we cannot use blank sky observations that were taken in regions of the sky where the foreground N_H is different (not to mention other uncertainties due to different detector settings, particle radiation levels, etc.). Here we describe a method to use a local estimate of the sky background that takes properly into account vignetting and detector background issues.

To remove the detector background, we used archival observations which were taken in the same mode as the NGC 253 observations, but where the filter wheel was closed. To avoid effects due to changes in the detector settings, or changes of the detector performance due to other reasons, we chose the closed observations to be as close as possible in time to the NGC 253 observations. The closed observations we used for observation 1 and 4 are: revolution 59, obs. id. 0122320701, exposure S003 (50.5 ks) and revolution 732, obs. id. 0160362801, exposure S005 (38.6 ks), respectively. To ensure, that there are as little as possible differences between the source observation and the closed observation, we removed bad columns and bad pixels both in the NGC 253 and closed observation. Additionally, the closed observations may have been taken when the spacecraft was exposed to a different particle radiation level than the one present during observations 1 or 4. The *XMM-Newton* house keeping file contains information on how many CCD rows per time unit were rejected due to a possible minimum ionising particle (MIP) event, which is a direct estimator of the average radiation level. We used these values (see Table C.1), to rescale the count rate of the closed observations.

We used Out-of-Time spectra from the source and background region to correct for contribution from Out-of-Time events. When one subtracts a closed observation spectrum from a Out-of-Time corrected spectrum, one actually removes the Out-of-Time spectrum of the detector background twice. This is corrected in our method by adding again the Out-of-Time spectra of the detector background.

We corrected the background region spectrum for Out-of-Time events and the detector background and applied the vignetting correction in each energy bin as a function of off-axis

$$\begin{aligned}
B(E) = & \underbrace{S_{\text{obs}}^{\text{OOT}}(E) \times f}_{\text{Out-of-Time events}} + \underbrace{S_{\text{det}}(E) \frac{R_{\text{obs}}}{R_{\text{det}}} \frac{t_{\text{obs}}}{t_{\text{det}}}}_{\text{detector background}} - \underbrace{S_{\text{det}}^{\text{OOT}}(E) \frac{R_{\text{obs}}}{R_{\text{det}}} \frac{t_{\text{obs}}}{t_{\text{det}}} \times f}_{\text{detector Out-of-Time events}} + \\
& + \underbrace{\frac{V(E, \theta_S)}{V(E, \theta_B)} \frac{A_S}{A_B} \times \left(B_{\text{obs}}(E) - \underbrace{B_{\text{obs}}^{\text{OOT}}(E) \times f}_{\text{Out-of-Time events}} - \underbrace{B_{\text{det}}(E) \frac{R_{\text{obs}}}{R_{\text{det}}} \frac{t_{\text{obs}}}{t_{\text{det}}}}_{\text{detector background}} + \underbrace{B_{\text{det}}^{\text{OOT}}(E) \frac{R_{\text{obs}}}{R_{\text{det}}} \frac{t_{\text{obs}}}{t_{\text{det}}} \times f}_{\text{detector Out-of-time events}} \right)}_{\text{sky background}} \quad (C.1)
\end{aligned}$$

angle of the source and background spectrum. This gave us the sky background spectrum.

In all of the above steps, different exposure times and areas in the extraction regions have been accounted for. Since some of the components in the final background spectrum do have low number statistics, we used the conservative approximation to Poissonian errors $\sigma_N \approx 1 + \sqrt{0.75 + N}$ (Gehrels 1986). To avoid unjustified large errors, we roughly binned the spectrum before calculating errors. The resulting background subtracted spectrum then has a significance in each bin of at least 3σ . The errors were propagated properly and were included in the file with the final background spectrum. This spectrum can be used with XSPEC as a background spectrum.

The whole method can be summarised by Eq. C.1 with the following symbols:

- $B(E)$ is the counts at energy E in the background spectrum
- $B_{\text{obs}}(E)$ is the counts in the NGC 253 observation
- $S_{\text{det}}(E)$ is the counts from the detector background spectrum in the source region
- $B_{\text{obs}}(E)$ is the counts in the detector background spectrum in the background region
- $S_{\text{obs}}^{\text{OOT}}(E)$ are the counts in the Out-of-Time spectra in the source region
- $B_{\text{obs}}^{\text{OOT}}(E)$ are the counts in the Out-of-Time spectra in the background region
- t_{obs} is the exposure time in the NGC 253 observation
- t_{det} is the exposure time in the closed observation
- R_{obs} is the rejected line counter values (see Table C.1) in the NGC 253 observation
- R_{det} is the rejected line counter values (see Table C.1) in the closed observation
- A_S is the area in the source region
- A_B is the area in the background region
- $V(E, \theta_S)$ is the vignetting value in the source region, depending on the offset angle θ and the energy E
- $V(E, \theta_B)$ is the vignetting value in the background region, depending on the offset angle θ and the energy E
- f is the fraction of Out-of-Time events in the corresponding mode of the observation

A comparison between this new method and the conventional method, that does not use the vignetting correction nor the closed observations, is shown in Fig. C.1 for two example spectra, both in observations 1 and 4. The single background components in the source and background region in observation 4 are shown in Fig. C.2. All figures show counts integrated over the extraction region. The counts in the background region

were rescaled to the source region area to be able to compare them to the source spectrum. Also, the counts in the closed observation were rescaled to the exposure time and radiation level in the source observation.

The differences between the new and the conventional method in terms of the resulting best fits are the following: In the majority of the tested cases, an additional power law component with $\Gamma \sim 0$ is required for the fit in the spectrum, obtained with the conventional method. The temperatures are consistent between both methods, but the resulting flux levels in the conventional method are higher. Differences in total flux values range between 2% and 22%. The effect between the two methods is highest in regions with low surface brightness. Here the background dominates and a correct treatment is crucial. As an example, the difference in flux in region 7 (low surface brightness) is 15% and 22%, for observations 1 and 4, respectively. Whereas in region 14 (high surface brightness), the differences are 2% and 3%.

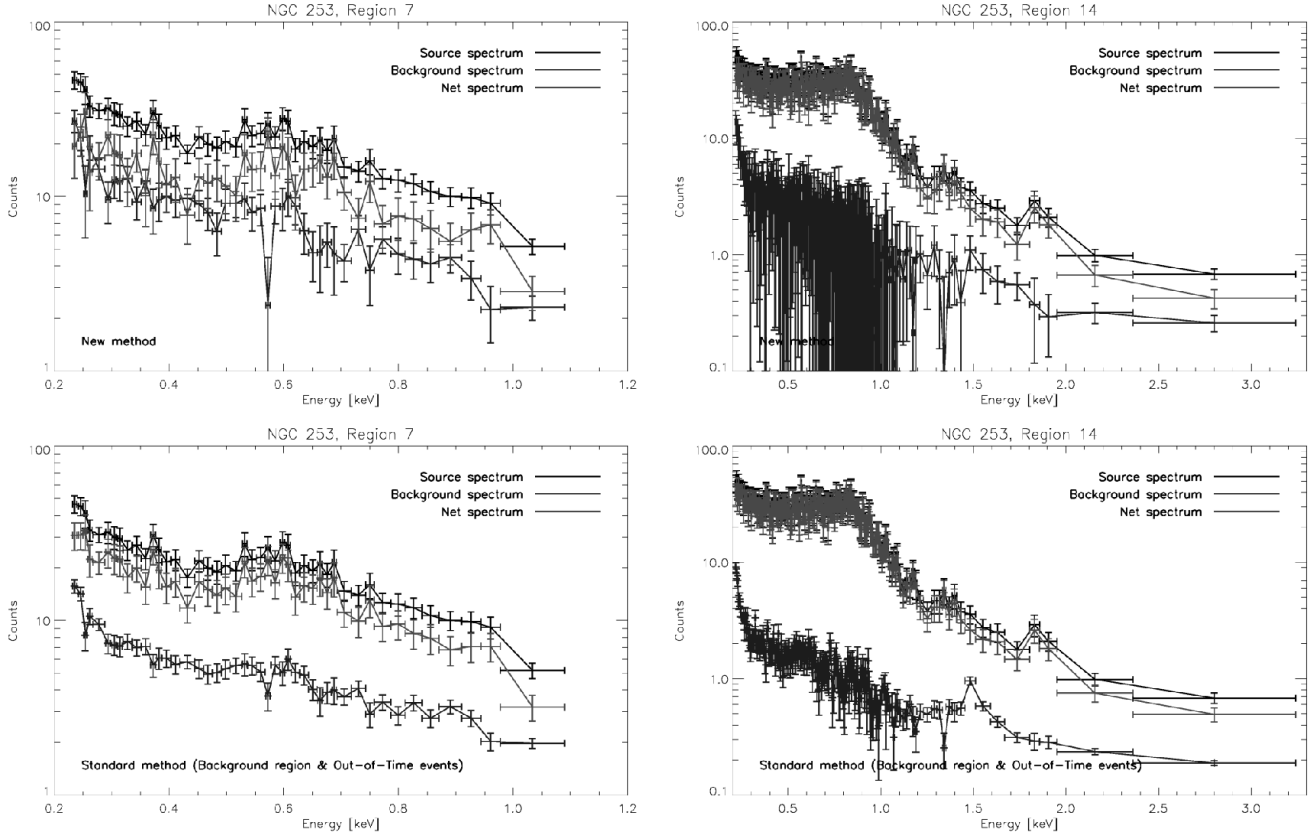


Fig. C.1. Comparison between the background subtraction on two examples (same source regions as in Fig 6). (*left*): the spectrum of region 7, (*right*): the spectrum of region 14. The top panel shows the new method, as described in this paper, the bottom panel shows the conventional method, where the raw background spectrum is used, and a correction for Out-of-Time events has been applied. We only show the spectra of observation 4 here, since these have the better statistics.

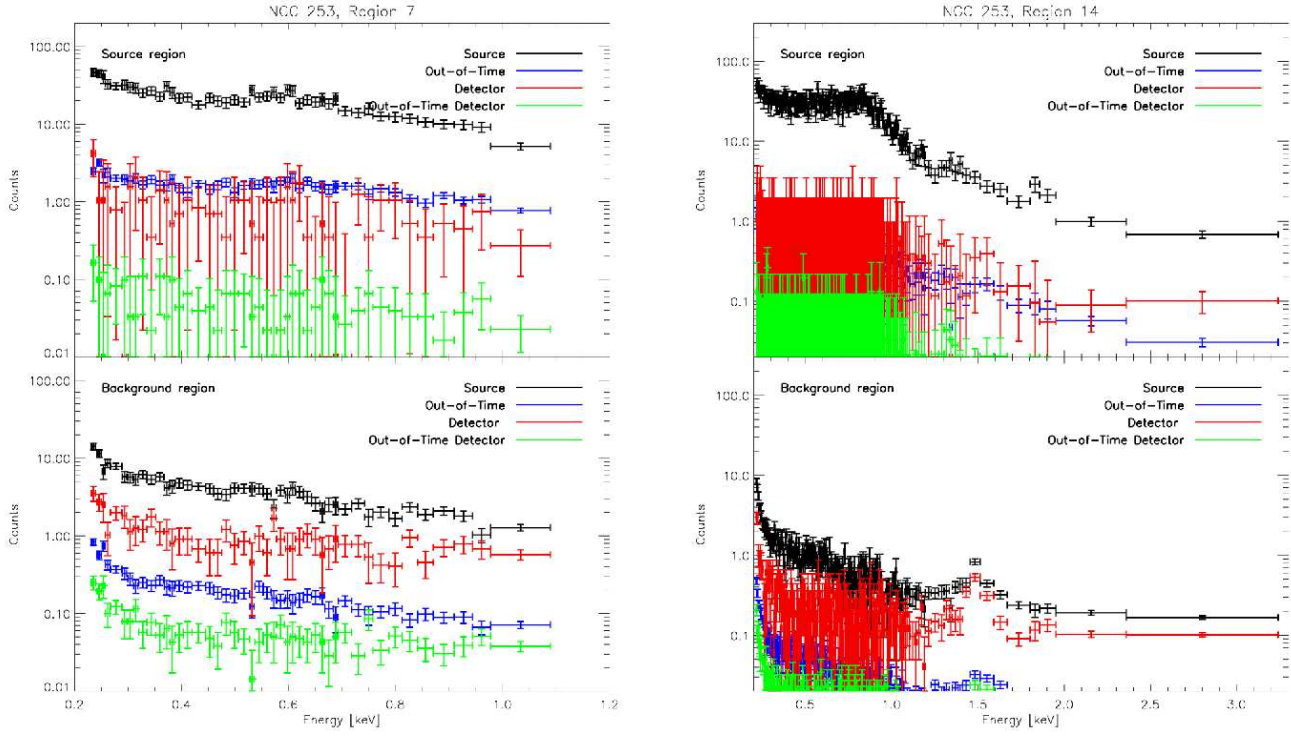


Fig. C.2. The single components that are part of the total background spectrum compared to the source spectrum. (*left*): Region 7, (*right*): Region 14, (*top*): components from the source region, (*bottom*): components from the background region. The single components were corrected for areas, exposure time, and radiation level, with respect to the source spectrum in the source region, but no vignetting correction was applied yet.